The Journal of Physical Chemistry Letters
Letter
pubs.acs.org/JPCL

Observation and Identification of a New OH Stretch Vibrational Band at the Surface of Ice

Wilbert J. Smit,[†,∥] Fujie Tang,[‡,¶] Yuki Nagata,[‡] M. Alejandra Sánchez,[‡] Taisuke Hasegawa,[§] Ellen H. G. Backus,[‡] Mischa Bonn,[‡] and Huib J. Bakker[*,†]

[†]AMOLF, Science Park 104, 1098 XG Amsterdam, The Netherlands
[‡]Max Planck Institute for Polymer Research, Ackermannweg 10, 55128 Mainz, Germany
[¶]International Center for Quantum Materials, Peking University, 5 Yiheyuan Road, Haidian, Beijing 100871, China
[§]Department of Chemistry, Graduate School of Science, Kyoto University, Sakyoku, Kyoto 606-8502, Japan

Supporting Information

ABSTRACT: We study the signatures of the OH stretch vibrations at the basal surface of ice using heterodyne-detected sum-frequency generation and molecular dynamics simulations. At 150 K, we observe seven distinct modes in the sum-frequency response, five of which have an analogue in the bulk, and two pure surface-specific modes at higher frequencies (~3530 and ~3700 cm^{-1}). The band at ~3530 cm^{-1} has not been reported previously. Using molecular dynamics simulations, we find that the ~3530 cm^{-1} band contains contributions from OH stretch vibrations of both fully coordinated interfacial water molecules and water molecules with two donor and one acceptor hydrogen bond.

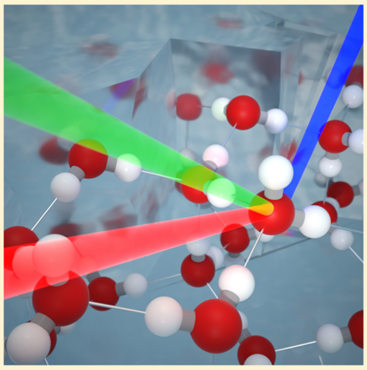

Ice plays a key geophysical role. Glaciers shape the Earth's surface, and ice particles in the atmosphere play a crucial role in lightning and the depletion of the ozone layer.[1−4] Ice has at least 16 distinct crystalline phases,[5] but the only thermodynamical stable phase that naturally occurs on the Earth's surface is hexagonal ice (ice I$_h$).[6] For ice I$_h$, the oxygen atoms lie on a wurtzite lattice and the hydrogens are located in-between the oxygen atoms following the Bernal−Fowler ice rules.[7] These rules state that each oxygen is covalently bonded to two hydrogen atoms and forms two hydrogen bonds with two neighboring hydrogen atoms and that the surrounding water molecules are oriented in such a way that only one hydrogen atom lays between each pair of oxygen atoms. At the surface, the crystal structure is terminated, leaving the outermost water molecules with an incomplete hydrogen bond configuration.

At low temperatures, the surface of ice is highly ordered; the basal plane of ice I$_h$ has full-bilayer termination, and the outer molecules have either a free OH group or an oxygen atom with a free lone electron pair.[8−10] At somewhat elevated temperatures (reported to be 180−200 K[11,12]), surface disorder sets in, finally resulting in premelting of the surface.[13−15] This premelted layer has been reported to be important for processes such as glacier motion, frost heave, and chemical reactions taking place at the surface of ice particles in the atmosphere.[2,3]

It is highly challenging to acquire detailed molecular-scale insights into the properties of the surface of ice. In most practical situations, the surface region is very thin compared to the bulk, which implies that a technique with high surface-specificity is needed to obtain unambiguous information on the surface. Furthermore, the technique should be minimally invasive because the ice surface can be easily melted and irreversibly deformed.[13,16]

Sum-frequency generation (SFG) spectroscopy is a suitable technique for studying the surface of ice as it is noninvasive, highly surface-specific, and selective to molecular groups. Because SFG is an even-order ($\chi^{(2)}$) nonlinear optical process, SFG is bulk-forbidden for water and ice under the electric dipole approximation.[17,18] As the frequency of the OH stretch vibrations is strongly correlated with the strength of the hydrogen bonds,[19,20] the SFG spectrum of vibrations of water molecules at the ice surface can provide insight into the molecular configuration of the surface. The surface properties of ice have thus been studied with conventional intensity SFG spectroscopy,[12,15,17,21−25] and the results have been compared with molecular dynamics (MD) simulations.[15,26−28]

In this Letter, we report on a study of the ice surface with heterodyne-detected SFG (HD-SFG). In this technique, the sum-frequency signal is interfered with a local oscillator field, thus enabling a direct determination of the amplitude and phase of the generated sum-frequency electric field. The SFG electric field can be directly related to the amplitude and phase of the

Received: May 23, 2017
Accepted: July 17, 2017
Published: July 17, 2017

DOI: 10.1021/acs.jpclett.7b01295
J. Phys. Chem. Lett. 2017, 8, 3656−3660

second-order susceptibility $\chi^{(2)}$ (in conventional intensity SFG, $|\chi^{(2)}|^2$ is measured). As a result, HD-SFG provides not only the response spectrum of the molecular vibrations at the surface but also their orientation. Here, we specifically make use of the fact that HD-SFG allows access to the imaginary part of $\chi^{(2)}$, to which different modes simply contribute additively. This allows a straightforward analysis of the surface vibrational response in terms of different modes. In combination with MD simulations, we thus investigate the properties of the basal surface of ice between 150 and 245 K through its different vibrational modes.

The basal surface of ice I_h is schematically depicted in Figure 1. The water molecules can be classified into different categories following the number of hydrogen bonds that a water molecule donates (D) or accepts (A); for instance, DAA molecules are water molecules of which one of the OH groups donates a hydrogen bond and of which the oxygen atom accepts two hydrogen bonds. For a perfectly structured basal face, the topmost water layer consists of 50% DAA and 50% DDA water molecules.[29]

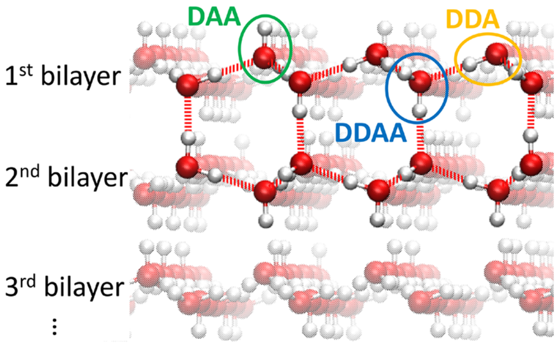

Figure 1. Fragment of the basal surface of ice I_h in its perfect form. The bilayers are formed by water molecules in a chair configuration. The upper part of the first bilayer consists of water molecules with a free OH group (DAA) and of water molecules with a lone pair (DDA). All other water molecules are fully coordinated (DDAA). The bilayers are interconnected by stitching bonds.

The growth and handling of single-crystal ice and the experimental setup are described in the Supporting Information. In Figure 2a, we present the real and imaginary parts of the $\chi^{(2)}$ of the basal face of ice at 150 K. The imaginary part of $\chi^{(2)}$ contains direct information on the vibrational resonances. The real part of $\chi^{(2)}$ complements the imaginary part and also contains a small negative nonresonant background contribution.

Below 3500 cm^{-1}, five resonances are clearly distinguishable in the Im $\chi^{(2)}$ response. From low to high frequency, the first resonance shows up as a dispersive-like feature at 3110 cm^{-1} (discussed in more detail below); the additional four appear at 3150, 3228, 3350, and 3420 cm^{-1} (as indicated by the vertical dashed lines). The Raman and infrared absorption spectra of bulk ice presented in Figure 2b,c show similarities with the $\chi^{(2)}$ spectrum of Figure 2a. Note that the $\chi^{(2)}$ associated with a vibrational resonance is proportional to the product of its Raman transition polarizability and its infrared transition dipole moment. Together, the Raman and infrared bulk spectra reproduce the five main resonances,[30] which we label from low to high frequency by I–V. Bands I, III, IV, and V are visible in the Raman spectrum, and bands II and III are observable in the infrared spectrum. All of these bands have been assigned to delocalized OH vibrations[30−33] and can thus not be assigned to particular water molecules with specific hydrogen bond configurations. According to the simulation results of Li and Skinner,[30] bands II and V result from strong intermolecular coupling between OH stretch vibrations on neighboring water molecules for which no other hydrogen atom is located in-between the coupled OH groups. Bands III and IV result from the weaker intermolecular coupling between OH stretch vibrations for which there is one other hydrogen atom located in-between the two OH groups. The infrared spectrum contains an additional shoulder in-between the frequency positions of bands IV and V. According to the simulation results of Li and Skinner,[30] this shoulder has the same origin as band IV in the Raman spectrum.

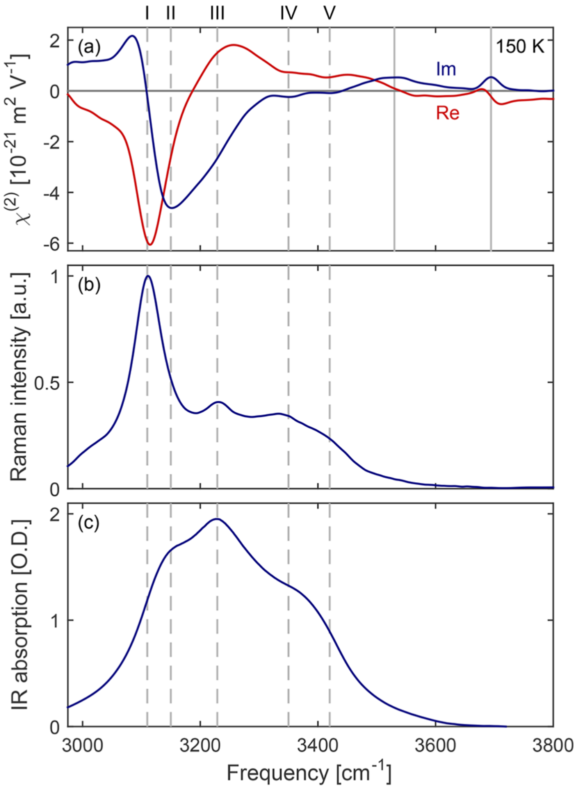

Figure 2. Experimental comparison between the SFG spectrum and the bulk Raman and infrared absorption spectra at 150 K. (a) Real and imaginary parts of the second-order susceptibility element $\chi^{(2)}_{xxz}$ of the basal surface of ice. (b) Unpolarized Raman spectrum of polycrystalline ice. (c) Infrared absorption spectrum of polycrystalline ice.

Bands II, III, IV, and V all appear as peaks with negative amplitudes in the Im $\chi^{(2)}$ spectrum. In contrast, band I does not coincide with a maximum or minimum in the Im $\chi^{(2)}$ spectrum but rather with a strong peak in the Re $\chi^{(2)}$ spectrum. The strong Raman band I has been assigned to a collective in-phase OH stretch vibration,[30,33,34] and SFG experiments using the polarization null-angle method[17,35] have shown that band I (with a frequency of 3098 cm^{-1} at 113 K) contains a significant quadrupole contribution. As a result, mode I has been assigned to water molecules forming bilayer-stitching hydrogen bonds, which thus constitute neighboring oppositely aligned dipoles.[35] The significant quadrupole bulk response[23,28,35] leads to a 90° phase shift of this mode in the $\chi^{(2)}$ response with respect to a pure surface mode.[36−38] As a result, band I leads to a maximum negative amplitude at 3100 cm^{-1} in the real part of $\chi^{(2)}$ and a dispersive line shape for Im $\chi^{(2)}$ around 3100 cm^{-1}. The quadrupolar character of the signal of band I implies that the

DOI: 10.1021/acs.jpclett.7b01295
J. Phys. Chem. Lett. 2017, 8, 3656−3660

generated SFG light can originate from both the bulk and the interface. It has been theoretically shown that a bulk quadrupolar contribution can be distinguished from an interfacial contribution by varying the optical geometry of the experiment.[39] This will be the subject of future study.

In Figure 3, we present HD-SFG spectra of the basal ice surface at different temperatures in the range of 150−245 K. From the measured real and imaginary $\chi^{(2)}$, we construct $|\chi^{(2)}|^2$ spectra. The spectral features of the $\chi^{(2)}$ spectrum become less pronounced at higher temperatures. Modes I−III merge into a single broad band. A similar effect is observed for modes IV and V. These modes broaden and merge into a single broad band at higher temperatures. The overall spectrum shifts to higher frequencies when the temperature increases, which can be explained from a weakening of the hydrogen bonds. The amplitude of the low-frequency modes I−III decreases when the temperature rises. In particular, the bilayer-stitching mode (I) exhibits a strong temperature dependence and has been reported to even gain further strength below 150 K.[22] The decrease in the $\chi^{(2)}$ response of mode I with increasing temperature can be explained from a decrease in vibrational coupling due to an increase of the thermal fluctuations.[26,27] As a result, the depth over which the SFG signal is generated decreases with increasing temperature, thereby weakening the signal.

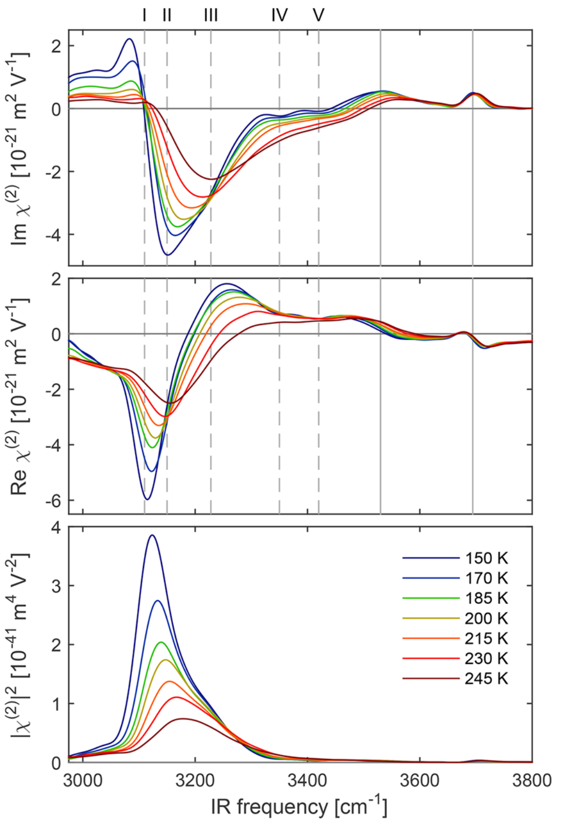

Figure 3. *xxz*-Component of the experimental second-order susceptibility $\chi^{(2)}$ of the basal ice−air interface at different temperatures. The top panel shows the imaginary component (Im $\chi^{(2)}$), the central panel the real component (Re $\chi^{(2)}$), and the bottom panel the squared amplitude ($|\chi^{(2)}|^2$).

The Im $\chi^{(2)}$ spectra also exhibit two bands at ~3530 and ~3700 cm^{-1} (as indicated by the vertical solid lines in Figures 2 and 3) that are not apparent from the infrared and Raman bulk spectra. The resonance at ~3700 cm^{-1} has been assigned to the stretching vibration of free OH groups sticking out of the surface.[12] The low amplitude of the band at ~3530 cm^{-1} in the Im $\chi^{(2)}$ spectra makes it difficult to distinguish this band in the constructed $|\chi^{(2)}|^2$ spectra. As a result, this band has not been reported previously.

To assign the band at ~3530 cm^{-1}, we performed MD simulations of the ice−air interface using a slab model (see the Supporting Information for details), focusing on the spectral region of 3400−3800 cm^{-1}. The simulation cell contains 1344 water molecules, which form 12 bilayers. Water molecules are modeled with the POLI2VS force field,[40] which can reproduce the SFG signatures of the liquid water−air interface including a shoulder band at ~3600 cm^{-1}.[41] SFG spectra are generated by computing the time correlation function of the dipole moment and the polarizability[42] obtained from the MD simulations. The surface response of the 3400−3800 cm^{-1} region is found to be scarcely influenced by intermolecular couplings (see Figure S5 in the Supporting Information).[43] As such, SFG spectra are calculated without cross-correlation terms in order to allow for a decomposition of the spectral response in this frequency region into the responses of different hydrogen-bonded types of water molecules.

In Figure 4, we show a comparison of the experimental and simulated spectra and the contributions of different hydrogen-bonded types of water molecules to the spectral response. Water molecules with a dangling OH group (DAA and DA) are responsible for the peak at ~3700 cm^{-1}. The broad band at around 3530 cm^{-1} is composed of contributions to Im $\chi^{(2)}$ from fully coordinated DDAA molecules and from DDA water molecules with opposite sign. The positive contribution from DDAA molecules is located at around 3475−3500 cm^{-1} and has a slightly higher frequency than the negative contribution from DDA water molecules at around 3440−3480 cm^{-1}. In addition, the amplitude of the DDAA molecules dominates over the amplitude of the DDA molecules, finally resulting in a net positive band near 3530 cm^{-1}.

Both the experiment and the simulation show that the amplitude of the ~3530 cm^{-1} band decreases when the temperature increases. The MD simulations show that this temperature dependence is caused by a decrease in amplitude of both the positive DDAA band as well as the negative DDA band. The amplitude of the DDA band exhibits a stronger decrease with temperature than the amplitude of the DDAA band, which follows from the fact that the DDA molecules are located in the outermost layer of the ice surface (see Figure 1) and thus are more strongly affected by an increase in surface disorder than the DDAA molecules. With increasing temperature, the 3530 cm^{-1} band shifts to higher frequency as a result of a weakening of the hydrogen bonds of both the DDA and the DDAA water species.[44]

The Im $\chi^{(2)}$ contribution of the DDAA molecules to the ~3530 cm^{-1} band arises from their asymmetric OH stretch vibration, whereas the Im $\chi^{(2)}$ response of the DDA molecules results from their symmetric OH stretch vibration. The negative sign of the latter response reflects the net orientation of the DDA molecules with both OH groups pointing toward the bulk. The DDA molecules also have an asymmetric stretch vibration that leads to a positive Im $\chi^{(2)}$ signal at ~3590 cm^{-1}. This band has zero amplitude at 150 K but acquires strength at elevated temperatures. For a perfectly ordered ice surface, the antisymmetric mode would be oriented parallel to the surface (see Figure 1) and would thus not contribute to the $\chi^{(2)}$

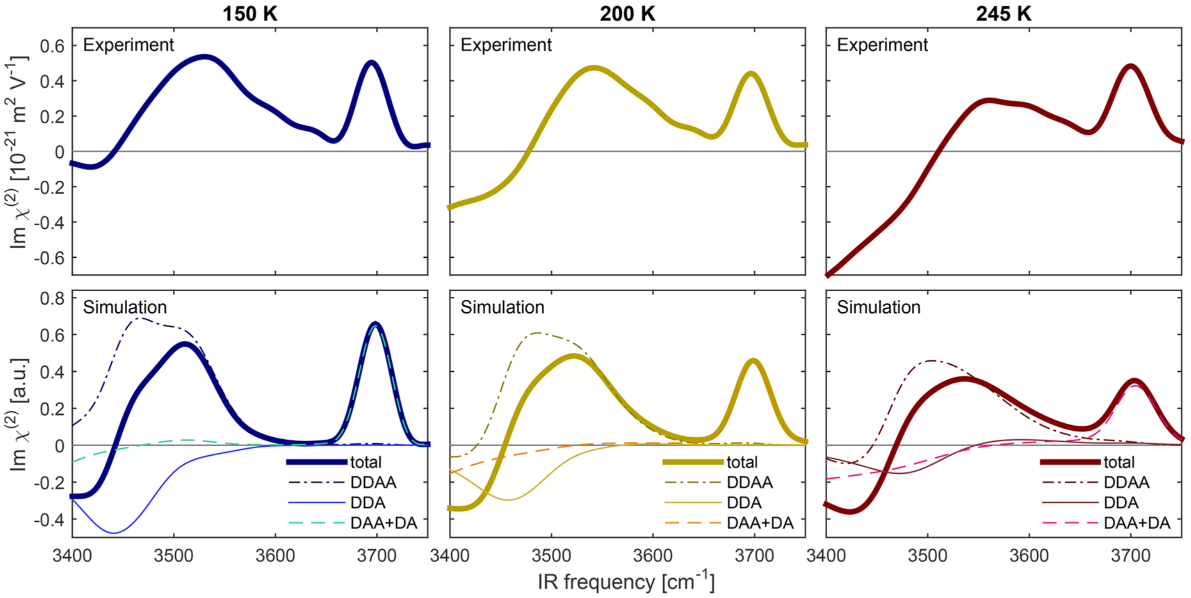

Figure 4. Spectral decomposition of the sum-frequency spectrum at 150, 200, and 245 K. The experimentally obtained spectra are shown in the top panels, and the simulated autocorrelation spectra are shown in the bottom panels. The simulated $\chi^{(2)}$ spectrum (heavy lines) can be decomposed into contributions from fully coordinated water molecules (DDAA, dashed−dotted lines), from water molecules with a dangling OH group (DAA and DA, dashed lines), and from water molecules with a free electron pair and two donor hydrogen bonds (DDA, solid lines).

spectrum. The observation of a nonzero amplitude of this mode and an increase of its amplitude with temperature can be well explained from an increasing disorder of the surface and thus of the orientation of the DDA water molecules. This result is consistent with the observations for the liquid water−air surface, for which a positive Im $\chi^{(2)}$ band has been observed at ∼3620 cm^{-1} and that has been attributed to the same mode.[44−46]

In conclusion, we studied the surface structure of the basal surface of ice by combining HD-SFG spectroscopy with MD simulations. We measured spectra in the OH stretch frequency range in the temperature range of 150−245 K. At 150 K, the experimentally obtained sum-frequency spectra exhibit five distinct bands in the range of 3000−3450 cm^{-1}, which correspond well to bands in the infrared and Raman bulk spectra. The sum-frequency spectrum also contains two bands with positive amplitude at ∼3530 and ∼3700 cm^{-1}. The MD simulations show that these bands can be identified as surface modes. We find that the ∼3530 cm^{-1} band contains contributions of the symmetric OH stretch vibrations of DDA water molecules and the asymmetric OH stretch vibrations of DDAA water molecules that have opposite signs. With increasing temperature, this band decreases in amplitude and shifts to higher frequency.

■ ASSOCIATED CONTENT

Ⓢ Supporting Information

The Supporting Information is available free of charge on the ACS Publications website at DOI: 10.1021/acs.jpclett.7b01295.

> Experimental details: single-crystal ice growth and temperature cell, experimental SFG setup and data analysis, effect of laser-induced heating, and measurement of bulk Raman and infrared spectra; Simulation protocols: MD simulation, calculation of SFG spectra, effects of intermolecular vibrational coupling on the SFG spectra, decomposition of SFG spectra, and hydrogen bond definition (PDF)

■ AUTHOR INFORMATION

Corresponding Author

*E-mail: bakker@amolf.nl.

ORCID

Wilbert J. Smit: 0000-0002-0543-7258
Mischa Bonn: 0000-0001-6851-8453

Present Address

[‖]W.J.S.: Laboratoire Sciences et Ingénierie de la Matière Molle, ESPCI Paris, PSL Research University, CNRS UMR 7615, 10 rue Vauquelin, 75005 Paris, France.

Notes

The authors declare no competing financial interest.

■ ACKNOWLEDGMENTS

This work is part of the research programme of The Netherlands Organisation for Scientific Research (NWO) and was performed at the research institute AMOLF. We thank Walter Scholdei for the Raman measurements.

■ REFERENCES

(1) Dash, J. G.; Fu, H.; Wettlaufer, J. S. The premelting of ice and its environmental consequences. *Rep. Prog. Phys.* **1995**, *58*, 115.

(2) Dash, J. G.; Rempel, A. W.; Wettlaufer, J. S. The physics of premelted ice and its geophysical consequences. *Rev. Mod. Phys.* **2006**, *78*, 695−741.

(3) Molina, M. J.; Tso, T.-L.; Molina, L. T.; Wang, F. C.-Y. Antarctic Stratospheric Chemistry of Chlorine Nitrate, Hydrogen Chloride, and Ice: Release of Active Chlorine. *Science* **1987**, *238*, 1253−1257.

(4) Bolton, K.; Pettersson, J. B. C. Ice-Catalyzed Ionization of Hydrochloric Acid. *J. Am. Chem. Soc.* **2001**, *123*, 7360−7363.

(5) Falenty, A.; Hansen, T. C.; Kuhs, W. F. Formation and properties of ice XVI obtained by emptying a type sII clathrate hydrate. *Nature* **2014**, *516*, 231−233.

(6) Murray, B. J.; Knopf, D. A.; Bertram, A. K. The formation of cubic ice under conditions relevant to Earth's atmosphere. *Nature* **2005**, *434*, 202−205.

(7) Bernal, J. D.; Fowler, R. H. A Theory of Water and Ionic Solution, with Particular Reference to Hydrogen and Hydroxyl Ions. *J. Chem. Phys.* **1933**, *1*, 515−548.

(8) Materer, N.; et al. Molecular surface structure of ice(0001): dynamical low-energy electron diffraction, total-energy calculations and molecular dynamics simulations. *Surf. Sci.* **1997**, *381*, 190−210.

(9) Braun, J.; Glebov, A.; Graham, A. P.; Menzel, A.; Toennies, J. P. Structure and Phonons of the Ice Surface. *Phys. Rev. Lett.* **1998**, *80*, 2638−2641.

(10) Glebov, A.; Graham, A. P.; Menzel, A.; Toennies, J. P.; Senet, P. A helium atom scattering study of the structure and phonon dynamics of the ice surface. *J. Chem. Phys.* **2000**, *112*, 11011−11022.

(11) Suter, M. T.; Andersson, P. U.; Pettersson, J. B. C. Surface properties of water ice at 150−191 K studied by elastic helium scattering. *J. Chem. Phys.* **2006**, *125*, 174704.

(12) Wei, X.; Miranda, P. B.; Shen, Y. R. Surface Vibrational Spectroscopic Study of Surface Melting of Ice. *Phys. Rev. Lett.* **2001**, *86*, 1554−1557.

(13) Li, Y.; Somorjai, G. A. Surface Premelting of Ice. *J. Phys. Chem. C* **2007**, *111*, 9631−9637.

(14) Björneholm, O.; Hansen, M. H.; Hodgson, A.; Liu, L.-M.; Limmer, D. T.; Michaelides, A.; Pedevilla, P.; Rossmeisl, J.; Shen, H.; Tocci, G.; et al. Water at Interfaces. *Chem. Rev.* **2016**, *116*, 7698−7726.

(15) Sánchez, M. A.; Kling, T.; Ishiyama, T.; van Zadel, M.-J.; Bisson, P. J.; Mezger, M.; Jochum, M. N.; Cyran, J. D.; Smit, W. J.; Bakker, H. J.; et al. Experimental and theoretical evidence for bilayer-by-bilayer surface melting of crystalline ice. *Proc. Natl. Acad. Sci. U. S. A.* **2017**, *114*, 227−232.

(16) Goertz, M. P.; Zhu, X.-Y.; Houston, J. E. Exploring the Liquid-like Layer on the Ice Surface. *Langmuir* **2009**, *25*, 6905−6908.

(17) Groenzin, H.; Li, I.; Shultz, M. J. Sum-frequency generation: Polarization surface spectroscopy analysis of the vibrational surface modes on the basal face of ice I_h. *J. Chem. Phys.* **2008**, *128*, 214510.

(18) Shen, Y. R. Phase-Sensitive Sum-Frequency Spectroscopy. *Annu. Rev. Phys. Chem.* **2013**, *64*, 129−150.

(19) Fecko, C. J.; Eaves, J. D.; Loparo, J. J.; Tokmakoff, A.; Geissler, P. L. Ultrafast hydrogen-bond dynamics in the infrared spectroscopy of water. *Science* **2003**, *301*, 1698−1702.

(20) Bakker, H. J.; Skinner, J. L. Vibrational Spectroscopy as a Probe of Structure and Dynamics in Liquid Water. *Chem. Rev.* **2010**, *110*, 1498−1517.

(21) Wei, X.; Miranda, P. B.; Zhang, C.; Shen, Y. R. Sum-frequency spectroscopic studies of ice interfaces. *Phys. Rev. B: Condens. Matter Mater. Phys.* **2002**, *66*, 085401.

(22) Groenzin, H.; Li, I.; Buch, V.; Shultz, M. J. The single-crystal, basal face of ice I_h investigated with sum frequency generation. *J. Chem. Phys.* **2007**, *127*, 214502.

(23) Li Barnett, I.; Groenzin, H.; Shultz, M. J. Hydrogen Bonding in the Hexagonal Ice Surface. *J. Phys. Chem. A* **2011**, *115*, 6039−6045.

(24) Bisson, P. J.; Shultz, M. J. Hydrogen Bonding in the Prism Face of Ice Ih via Sum Frequency Vibrational Spectroscopy. *J. Phys. Chem. A* **2013**, *117*, 6116−6125.

(25) Smolentsev, N.; Smit, W. J.; Bakker, H. J.; Roke, S. The interfacial structure of water droplets in a hydrophobic liquid. *Nat. Commun.* **2017**, *8*, 15548.

(26) Ishiyama, T.; Takahashi, H.; Morita, A. Origin of Vibrational Spectroscopic Response at Ice Surface. *J. Phys. Chem. Lett.* **2012**, *3*, 3001−3006.

(27) Ishiyama, T.; Morita, A. A direct evidence of vibrationally delocalized response at ice surface. *J. Chem. Phys.* **2014**, *141*, 18C503.

(28) Wan, Q.; Galli, G. First-Principles Framework to Compute Sum-Frequency Generation Vibrational Spectra of Semiconductors and Insulators. *Phys. Rev. Lett.* **2015**, *115*, 246404.

(29) Buch, V.; Groenzin, H.; Li, I.; Shultz, M. J.; Tosatti, E. *Proc. Natl. Acad. Sci. U. S. A.* **2008**, *105*, 5969−5974.

(30) Li, F.; Skinner, J. L. Infrared and Raman line shapes for ice Ih. II. H_2O and D_2O. *J. Chem. Phys.* **2010**, *133*, 244504.

(31) Bergren, M. S.; Rice, S. A. An Improved analysis of the OH stretching region of the vibrational spectrum of Ice Ih. *J. Chem. Phys.* **1982**, *77*, 583−602.

(32) Wojcik, M. J.; Buch, V.; Devlin, J. P. Spectra of isotopic ice mixtures. *J. Chem. Phys.* **1993**, *99*, 2332−2344.

(33) Shi, L.; Gruenbaum, S. M.; Skinner, J. L. Interpretation of IR and Raman Line Shapes for H_2O and D_2O Ice Ih. *J. Phys. Chem. B* **2012**, *116*, 13821−13830.

(34) Wong, P. T. T.; Whalley, E. Optical spectra of orientationally disordered crystal. V. Raman spectrum of ice Ih in the range 4000−350 cm^{-1}. *J. Chem. Phys.* **1975**, *62*, 2418−2425.

(35) Shultz, M. J.; Bisson, P.; Groenzin, H.; Li, I. Multiplexed polarization spectroscopy: Measuring surface hyperpolarizability orientation. *J. Chem. Phys.* **2010**, *133*, 054702.

(36) Wen, Y.-C.; Zha, S.; Liu, X.; Yang, S.; Guo, P.; Shi, G.; Fang, H.; Shen, Y. R.; Tian, C. Unveiling Microscopic Structures of Charged Water Interfaces by Surface-Specific Vibrational Spectroscopy. *Phys. Rev. Lett.* **2016**, *116*, 016101.

(37) Shen, Y. R. *Fundamentals of Sum-Frequency Spectroscopy*; Cambridge University Press, 2016.

(38) Sun, S.; Liang, R.; Xu, X.; Zhu, H.; Shen, Y. R.; Tian, C. Phase reference in phase-sensitive sum-frequency vibrational spectroscopy. *J. Chem. Phys.* **2016**, *144*, 244711.

(39) Shiratori, K.; Morita, A. Theory of quadrupole contributions from interface and bulk in second-order optical processes. *Bull. Chem. Soc. Jpn.* **2012**, *85*, 1061−1076.

(40) Hasegawa, T.; Tanimura, Y. A Polarizable Water Model for Intramolecular and Intermolecular Vibrational Spectroscopies. *J. Phys. Chem. B* **2011**, *115*, 5545−5553.

(41) Ohto, T.; Usui, K.; Hasegawa, T.; Bonn, M.; Nagata, Y. Toward ab initio molecular dynamics modeling for sum-frequency generation spectra; an efficient algorithm based on surface-specific velocity-velocity correlation function. *J. Chem. Phys.* **2015**, *143*, 124702.

(42) Morita, A.; Hynes, J. T. A Theoretical Analysis of the Sum Frequency Generation Spectrum of the Water Surface. II. Time-Dependent Approach. *J. Phys. Chem. B* **2002**, *106*, 673−685.

(43) Nagata, Y.; Mukamel, S. Vibrational Sum-Frequency Generation Spectroscopy at the Water/Lipid Interface: Molecular Dynamics Simulation Study. *J. Am. Chem. Soc.* **2010**, *132*, 6434−6442.

(44) Nagata, Y.; Hasegawa, T.; Backus, E. H. G.; Usui, K.; Yoshimune, S.; Ohto, T.; Bonn, M. The surface roughness, but not the water molecular orientation varies with temperature at the water−air interface. *Phys. Chem. Chem. Phys.* **2015**, *17*, 23559−23564.

(45) Schaefer, J.; Backus, E. H. G.; Nagata, Y.; Bonn, M. Both Inter- and Intramolecular Coupling of O−H Groups Determine the Vibrational Response of the Water/Air Interface. *J. Phys. Chem. Lett.* **2016**, *7*, 4591−4595.

(46) Stiopkin, I. V.; Weeraman, C.; Pieniazek, P. A.; Shalhout, F. Y.; Skinner, J. L.; Benderskii, A. V. Hydrogen bonding at the water surface revealed by isotopic dilution spectroscopy. *Nature* **2011**, *474*, 192−195.

DOI: 10.1021/acs.jpclett.7b01295
J. Phys. Chem. Lett. 2017, 8, 3656−3660

Supporting Information

Observation and Identification of a New OH Stretch Vibrational Band at the Surface of Ice

Wilbert J. Smit,[†,‖] Fujie Tang,[‡,¶] Yuki Nagata,[‡] M. Alejandra Sánchez,[‡] Taisuke Hasegawa,[§] Ellen H. G. Backus,[‡] Mischa Bonn,[‡] and Huib J. Bakker[*,†]

†*AMOLF, Science Park 104, 1098 XG Amsterdam, The Netherlands*

‡*Max Planck Institute for Polymer Research, Ackermannweg 10, 55128 Mainz, Germany*

¶*International Center for Quantum Materials, Peking University, 5 Yiheyuan Road, Haidian, Beijing 100871, China*

§*Department of Chemistry, Graduate School of Science, Kyoto University, Sakyoku, Kyoto 606-8502, Japan*

‖*Current address: Laboratoire Sciences et Ingénierie de la Matière Molle, ESPCI Paris, PSL Research University, CNRS UMR 7615, 10 rue Vauquelin, 75005 Paris, France*

E-mail: bakker@amolf.nl

S1 Experimental Details

S1.1 Single Crystal Ice Growth and Temperature Cell

Single-crystal ice is grown by applying the method of seed extraction from the melt:[1] A single crystal seed is frozen to a copper pin. The copper pin is cooled by a processor cooler (LD PC-V2) and the temperature is set to 270 K by adjusting the current through a resistance. The surface of the seed is molten by a heat gun. Next the seed is dipped in a pan with ultrapure water maintained at 273.6 K (i.e. 0.5 K above the melting point) and allowed to grow in the melt. After one hour, the seed is pulled from the melt with a speed of 5 mm/hour. While pulling, the temperature of the copper pin is gradually decreased to 240 K. After 10 hours, a crystal of height ∼50 mm and diameter ∼70 mm results (Fig. S1a). The crystal is stored in a freezer before further handling.

The ice crystal is cut into parts by a bandsaw (Proxxon MBS 240/E) with a nickel-plated saw. One piece is frozen to an aluminum bar. A slice is cut off to determine the orientation of

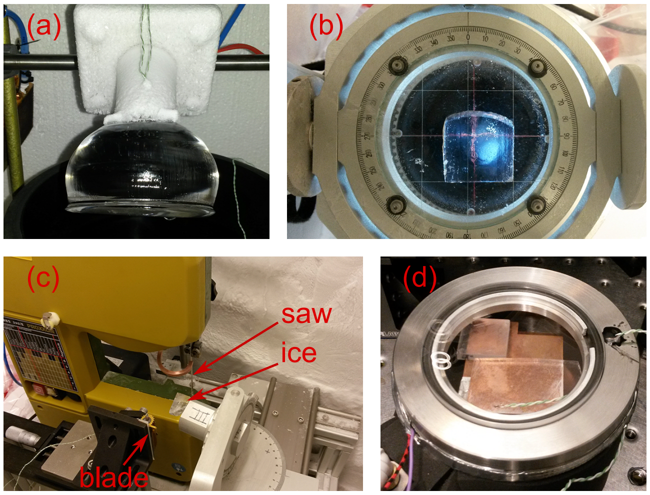

Figure S1: Ice growth and sample preparation. (a) Monocrystalline ice is grown by seed extraction from the melt. (b) The basal plane orientation is determined using a Rigsby stage. (c) Correctly oriented ice is shaved by a blade to smoothen the surface. Subsequently the sample is cut off by a bandsaw. (d) The ice sample in the sample cell. A thermocouple on the ice monitors the surface temperature. A z-cut quartz crystal is placed adjacent to the ice for reference purposes.

the basal plane using a Rigsby stage (Fig. S1b) following the routine described by Fairbairn.[2] Next the ice is cut in such a way that its optical axis is oriented perpendicular to the surface. A smooth surface is obtained by repeatedly shaving the ice using a blade of cemented carbide (Fig. S1c). Best results are obtained by shaving at a freezer temperature of ∼270 K with the blade heated to ∼300 K. A piece of ∼4 mm thickness is cut off and used in the experiment.

The SFG measurements are carried out using a closed temperature cell that is cooled with liquid N_2 and that allows transmittance of the laser beams through a CaF_2 window (Fig. S1d). The desired temperature is set by a heating foil resistance covered by a copper plate. The ice sample is placed on the copper plate. A temperature sensor is welded onto the ice surface with a water droplet in order to accurately monitor the surface temperature. For reference purposes a z-cut quartz crystal is placed adjacent to the ice. After positioning, the sample cell is thoroughly flushed with N_2 gas in order to remove the deposited frost that enters during the loading of the sample cell. The sample cell can be moved in the horizontal plane by two motorized actuators (Thorlabs) to prevent the accumulation of heat and damage of the ice crystal surface during the measurements (see Section S1.3).

S1.2 Experimental SFG Setup and Data Analysis

The laser source for the SFG experiments is a regenerative Ti:sapphire amplifier system (Coherent Legend) delivering 35 fs pulses with a pulse energy of 3.2 mJ at a wavelength of 798 nm (FWHM 70 nm) and a repetition rate of 1 kHz. The visible pulse is prepared by transmitting 20 % of the amplifier output through an etalon to reduce its spectral bandwidth, yielding a 15 μJ pulse with a FWHM of 0.9 nm (15 cm^{-1}). The infrared pulse is generated by the other 80 % of the amplifier output power in a home-built OPA with two BBO-based amplification stages. The generated signal and idler pulses are difference-frequency mixed in a $AgGaS_2$ crystal, producing 5 μJ broadband pulses centred at 3.0 μm (3300 cm^{-1}) with a FWHM of 600 nm (650 cm^{-1}). The visible and infrared pulses are set to s- and p-polarizations, respectively, using a combination of a $\lambda/2$-plate and a polarizer.

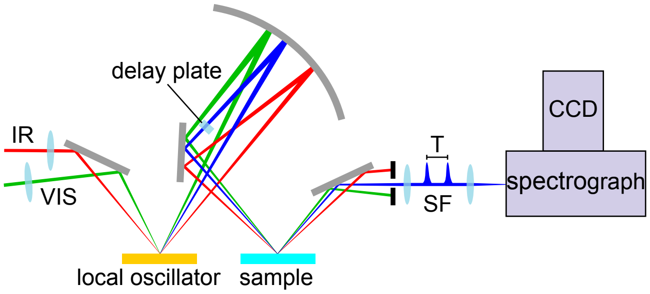

Figure S2: Schematic of the heterodyne-detected SFG setup. The infrared (IR) and visible (VIS) pulses are first sent in spatial overlap on a local oscillator (gold mirror) to generate broadband sum-frequency (SF) light. Next the pulses are refocused by a concave mirror onto the sample surface. The sum-frequency signal stemming from the local oscillator is delayed by a delay plate and creates an interference pattern with the sum-frequency signal generated at the sample, which is recorded by a spectrometer equipped with a CCD camera.

The geometry of the heterodyne-detected SFG setup is depicted in Fig. S2. First the infrared and visible pulses are spatially overlapped on a gold surface to generate broadband sum-frequency light, which is used as a local oscillator. Then the pulses are refocused by a concave mirror onto the sample surface with angles of incidence of 44° and 39° for the infrared and visible, respectively. The diameters at the sample position are $\sim$150 μm for the infrared and $\sim$200 μm for the visible laser beam. The sum-frequency signal stemming from the local oscillator is delayed by $T \simeq 2$ ps by transmission through a glass plate. The *s*-polarization component of the signal generated at the sample and the local oscillator are both sent into a spectrometer, where they are dispersed by a grating and recorded with a CCD camera for a total exposure time of $\sim$100 s. For each temperature, 3 to 5 spectra are recorded in succession and averaged. The signal from the sample and the local oscillator create an interference pattern. The detected intensity spectrum is thus proportional to:

$$\begin{aligned} I(\omega_{\mathrm{SF}}) \propto\ & |E_{\mathrm{sample}}(\omega_{\mathrm{SF}}) + r_{\mathrm{sample}}(\omega_{\mathrm{SF}}) E_{\mathrm{LO}}(\omega_{\mathrm{SF}}) \mathrm{e}^{i\omega_{\mathrm{SF}}T}|^2 \\ =\ & |E_{\mathrm{sample}}(\omega_{\mathrm{SF}})|^2 + |r_{\mathrm{sample}} E_{\mathrm{LO}}(\omega_{\mathrm{SF}})|^2 \\ & + r^*_{\mathrm{sample}}(\omega_{\mathrm{SF}}) E_{\mathrm{sample}}(\omega_{\mathrm{SF}}) E^*_{\mathrm{LO}}(\omega_{\mathrm{SF}}) \mathrm{e}^{-i\omega_{\mathrm{SF}}T} \\ & + r_{\mathrm{sample}}(\omega_{\mathrm{SF}}) E^*_{\mathrm{sample}}(\omega_{\mathrm{SF}}) E_{\mathrm{LO}}(\omega_{\mathrm{SF}}) \mathrm{e}^{i\omega_{\mathrm{SF}}T}, \end{aligned} \tag{S1}$$

where r is the reflection coefficient, and E_{LO} and E_{sample} are the sum-frequency fields of the local oscillator and sample, respectively. The cross terms are responsible for the interference pattern and contain the phase information. Because the cross terms carry a phase factor owing to the delay T, they can be isolated by Fourier filtering in the time domain.[3] The term with positive time is extracted and divided by the corresponding term of a reference spectrum measured on z-cut quartz. The resulting quotient is proportional to the ratio of the frequency-dependent second-order susceptibilities of the sample ($\chi^{(2)}_{\mathrm{sample}}$) and the frequency-independent susceptibility of quartz ($\chi^{(2)}_{\mathrm{quartz}}$):

$$\frac{r^*_{\mathrm{sample}} E_{\mathrm{sample}} E^*_{\mathrm{LO}} \mathrm{e}^{-i\omega_{\mathrm{SF}} T}}{r^*_{\mathrm{quartz}} E_{\mathrm{quartz}} E^*_{\mathrm{LO}} \mathrm{e}^{-i\omega_{\mathrm{SF}} T}} = \frac{r^*_{\mathrm{sample}} F_{\mathrm{sample}}}{r^*_{\mathrm{quartz}} F_{\mathrm{quartz}}} \frac{\chi^{(2)}_{\mathrm{sample}}}{i\chi^{(2)}_{\mathrm{quartz}}}. \tag{S2}$$

The F factors are dispersive constants comprising the product of geometrical factors and Fresnel factors.[3–5] The latter can be calculated using literature values of the optical constants.[6–8] For ice, the infrared optical constants are used that are determined at the closest temperature,[7] and the effective refractive index of the interfacial layer is calculated using a slab model.[9] The calculated magnitude and phase of the Fresnel factors are shown in Fig. S3. The factor i in front of $\chi^{(2)}_{\mathrm{quartz}}$ reflects the bulk origin of the quartz response, which has a 90° phase-shift with respect to a surface response.[5,10,11] The bulk $\chi^{(2)}$ value of quartz is taken to be $8 \cdot 10^{-13}$ m V^{-1} and the coherence length is calculated to be ∼40 nm for our experimental configuration.[12] The achieved $\chi^{(2)}_{\mathrm{sample}}$ is independent of experimental parameters. The *ssp*-polarization configuration of the sum-frequency, visible, and infrared beams yields the $\chi^{(2)}_{xxz}$ component, that consists of a projection of the Raman polarizability parallel to the surface plane and a projection of the infrared transition dipole moment perpendicular to the surface plane.

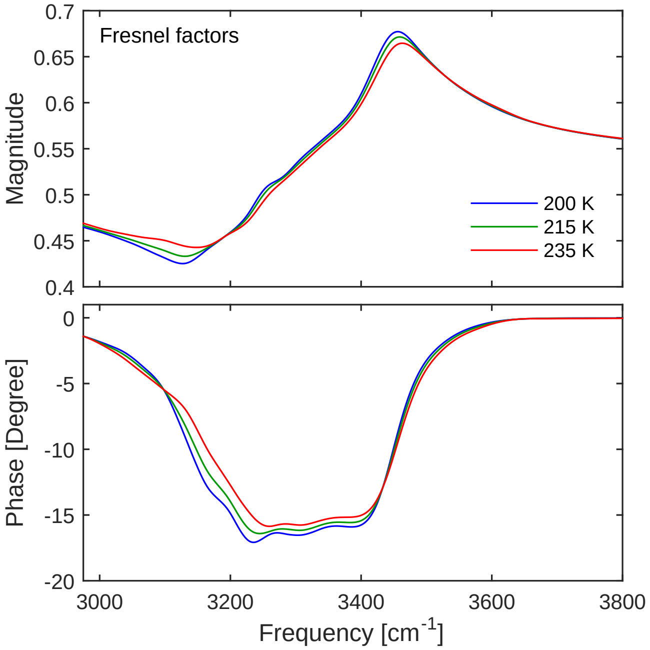

Figure S3: Fresnel factors of the ice–air interface for an *ssp*-polarization configuration at 200, 215, and 235 K.

S1.3 Effect of Laser-Induced Heating

In order to investigate the effect of laser-induced heating on the obtained SFG spectra of the ice surface, we vary the intensity of the infrared pulses and the speed of the actuators moving the sample. As can be seen in Fig. S4, the spectral shape remains constant under various intensity and moving speed conditions. Hence, we conclude that the heating effect of the laser pulses is negligible.

S1.4 Measurement of Bulk Raman and Infrared Spectra

Raman spectra are taken with a Bruker SENTERRA Raman microscope. Infrared absorption spectra are obtained with a PerkinElmer 881 double-beam IR spectrometer. The sample is prepared by pressing a water droplet between two windows. The sample is placed in a cryostat where the temperature is set.

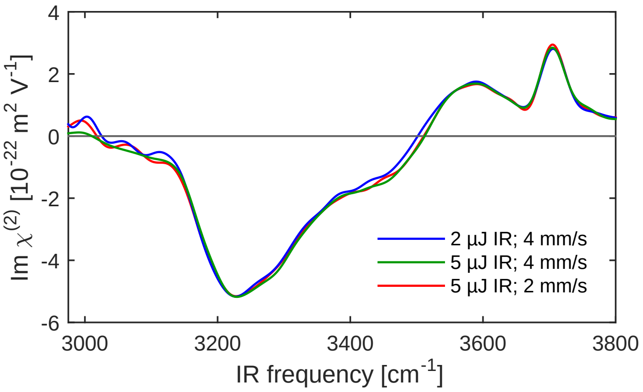

Figure S4: SFG spectra at various infrared intensities and moving speeds of the ice sample at ∼250 K. The sample is of a different cut than the one used in the main manuscript. Both a reduction in intensity of the infrared pulses from 5 μJ to 2 μJ as well as a reduction in the moving speed from 4 mm/s to 2 mm/s do not affect the spectral shape.

S2 Simulation Protocols

S2.1 Molecular Dynamics Simulation

We performed molecular dynamics (MD) simulation of the basal face of ice ($\mathrm{I_h}$) by using the POLI2VS force field model.[13] We used a slab model and three-dimensional periodic boundary conditions. This cell contains 1344 water molecules, forming 12 bilayers. The simulation cells are set to 31.471 Å × 31.149 Å × 60 Å at 150 K, 31.522 Å × 31.199 Å × 60 Å at 200 K, 31.584 Å × 31.260 Å × 60 Å at 245 K, respectively The charge–charge, charge–dipole, and dipole–dipole interactions are calculated with the Ewald method, while the charge–quadrupole, dipole–quadrupole, quadrupole–quadrupole, and short-range non-electrostatic interactions are smoothly truncated between 10 and 11.5 Å by a smoothing function. The reversible reference system propagator algorithm (r-RESPA) method in combination with second-order symplectic integrator was employed to describe the intermolecular interactions with a 0.4 fs time step, while the intramolecular motions are integrated by the sixth-order symplectic integrator with a 0.2 fs time step within the r-RESPA algorithm.[14,15] We constructed 25 independent systems at each temperature. To equilibrate each system at the targeted temperatures, we performed initial constant temperature (NVT) MD runs for 400 ps at 150 and 200 K, and for 250 ps at 245 K. The temperature is controlled using the Nosé–Hoover chain thermostat.[16] We then calculated NVT MD trajectories for total times of 7.0 ns, 15.0 ns, and 7.0 ns for the 150 K, 200 K, and 245 K systems, respectively, and we used the obtained trajectories to compute the SFG spectra. Note that a long MD trajectory for 200 K was needed to check the convergence of the calculated spectral features in the truncated response function formalism.[17] This is further discussed below.

S2.2 Calculation of SFG Spectra

The methodology to calculate the SFG spectra from the time correlation function of the dipole moment and polarizability has been reported in detail before.[18] Here, we outline the essence of these calculations. The SFG response of the ice surface can be calculated with the truncating response function:[17,18]

$$\chi^{\mathrm{res},(2)}_{\mathrm{xxz}}(\omega; r_t) = iQ(\omega) \int_0^{\tau} \mathrm{d}t\, R^{(2)}_{\mathrm{xxz}}(t; r_t) f(t) e^{-i\omega t}, \tag{S3}$$

where the z-axis is the surface normal and the xy-plane is the ice surface. The quantum correction factor $Q(\omega)$ is calculated by[19]

$$Q(\omega) = \frac{\hbar\omega}{k_{\mathrm{B}}T} \frac{1}{1 - \exp(-\hbar\omega/k_{\mathrm{B}}T)}, \tag{S4}$$

where T is the temperature, k_{B} is the Boltzmann constant. $f(t)$ is the Hann window function and is calculated by

$$f(t) = \begin{cases} \cos^2(\pi t/2\tau) & \text{for } 0 < t < \tau \\ 0 & \text{for } t \geq \tau \end{cases}, \tag{S5}$$

with a truncation time τ of the Fourier transformation. In this study, we used $\tau = 1.024$ ps for Fig. 4 in the main text, while we used a short τ of 0.424 ps for Fig. S5 to suppress the noise in the spectra. The time correlation function $R^{(2)}_{\mathrm{xxz}}(t;r_t)$ is calculated with

$$R^{(2)}_{\mathrm{xxz}}(t;r_t)=\left\langle\sum_i g_{sc}^3(z_i(0))\mu_{zi}(0)\alpha_{xxi}(t)+\right.$$
$$\left.\sum_i\sum_{j\neq i} g_{gc}(z_i(0))g_{sc}^2(z_j(0))\mu_{zi}(0)\alpha_{xxj}(t)g_t(r_{ij}(0);r_t)\right\rangle, \tag{S6}$$

where $\mu_{ai}(t)$ is the a-component of the molecular dipole moment and $\alpha_{abi}(t)$ is the ab-component of the molecular polarizability of water molecule i at time t. $g_t(r;r_t)$ is the term to control the cross-correlation terms with the cross-correlation cut-off radius of r_t. The definition of $g_t(r;r_t)$ is given by

$$g_t(r;r_t)=\begin{cases}1 & \text{for } r\leq r_t\\ 0 & \text{for } r>r_t\end{cases}. \tag{S7}$$

In order to avoid the cancellation of the dipole moments along the surface normal at the two ice surfaces, where the net orientations of water molecules are opposite, the dipole moment is multiplied by the screening function

$$g_{sc}(z)=\begin{cases}0 & \text{for } |z|\leq z_{c1}\\ \cos^2\left(\frac{\pi(|z|-z_{c2})}{2(z_{c1}-z_{c2})}\right) & \text{for } z_{c1}<|z|\leq z_{c2}\\ 1 & \text{for } z_{c2}<|z|\end{cases}, \tag{S8}$$

where z is the z-coordinate of the oxygen atom of a water molecule. We define the interfacial region for $z_{c2}\leq|z|$ and the bulk region as $|z|\leq z_{c1}$. The vibrational responses of water molecules is calculated in the interfacial region only through the screening function of $g_{sc}(z)$. Here, we set $z_{c1}=7$ Å and $z_{c2}=8$ Å, where the origin point was set to the center of mass of the system. The range of $z_{c1}\leq|z|\leq z_{c2}$ is located in-between two neighbouring bilayers in the bulk.

Nuclear quantum effects lead to a redshift of the vibrational signatures of the SFG response of ice.[20] Since no nuclear quantum effects are included in the current MD simulation, the resonant frequency is overestimated in the current simulated SFG spectra. To compensate for this, the frequency is scaled down by a factor of 0.96.[18,21]

S2.3 Effects of Intermolecular Vibrational Coupling on the SFG Spectra

We simulated SFG spectra at various cross-correlation truncation lengths r_t for ice at 200 K to examine the effects of the intermolecular vibrational coupling on the SFG spectra in the frequency region above 3400 cm^{-1}. The data are presented in Fig. S5. The results show that the calculated spectral features are not strongly dependent on the truncation length r_t, indicating that the intermolecular coupling of the OH stretch modes does not affect the ice SFG spectra above 3400 cm^{-1}. Indeed, negligible effects of intermolecular coupling on the high frequency side of the OH stretch band is consistent with previous results for the SFG spectrum of the liquid water–air interface.[22,23] The simulated spectra contain two positive bands at ∼3520 cm^{-1} and ∼3700 cm^{-1}, in agreement with the experimental spectra.

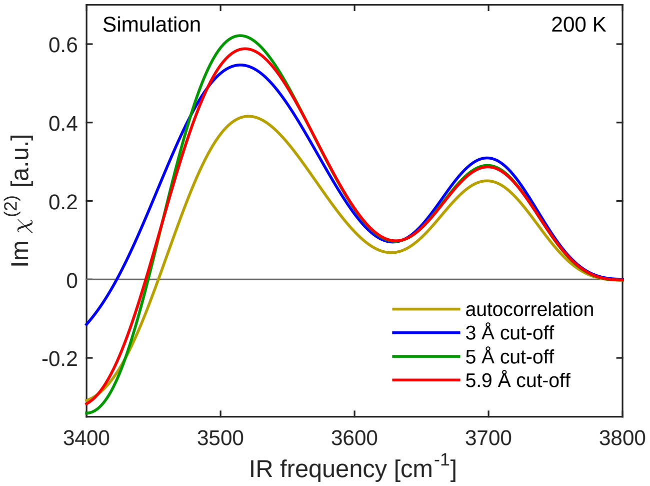

Figure S5: Simulated second-order susceptibility $\chi^{(2)}$ spectra of the 200 K ice–air interface at various cross-correlation truncation distances. The spectra are calculated using a truncation time of $\tau = 0.424$ ps for the correlation function (see Eq. S5).

S2.4 Decomposition of SFG Spectra

The SFG spectra calculated from the autocorrelation function can be decomposed in a straightforward manner with respect to the species of the water molecules. The response contributed by subensemble v of water molecules is given by

$$R^{(2)}_{\mathrm{xxz},v}(t; r_t = 0) = \left\langle \sum_i \theta_{i,v}(0) g^3_{sc}(z_i(0)) \mu_{zi}(0) \alpha_{xxi}(t) \right\rangle . \tag{S9}$$

Here $\theta_{i,v}(t)$ is unity when water molecule i is assigned to subensemble v at time t and zero otherwise.

S2.5 Hydrogen-Bond Definition

The water molecules are categorized in terms of their hydrogen-bonding configurations. We use as criteria for a hydrogen bond an OH$\cdots$O angle larger than 135° in combination with an O$\cdots$O distance smaller than 4.0 Å.

References

(1) Roos, D. S. Rapid production of single crystals of ice. *J. Glaciol.* **1975**, *14*, 975.

(2) Fairbairn, H. W. *Structural petrology of deformed rocks*; Addison-Wesley, 1954; pp 257–264.

(3) Nihonyanagi, S.; Yamaguchi, S.; Tahara, T. Direct evidence for orientational flip-flop of water molecules at charged interfaces: A heterodyne-detected vibrational sum frequency generation study. *J. Chem. Phys.* **2009**, *130*, 204704.

(4) Wang, H.-F.; Gan, W.; Lu, R.; Rao, Y.; Wu, B.-H. Quantitative spectral and orientational analysis in surface sum frequency generation vibrational spectroscopy (SFG-VS). *Int. Rev. Phys. Chem.* **2005**, *24*, 191–256.

(5) Fu, L.; Chen, S.-L.; Wang, H.-F. Validation of Spectra and Phase in Sub-1 cm^{-1} Resolution Sum-Frequency Generation Vibrational Spectroscopy through Internal Heterodyne Phase-Resolved Measurement. *J. Phys. Chem. B* **2016**, *120*, 1579–1589.

(6) Warren, S. G.; Brandt, R. E. Optical constants of ice from the ultraviolet to the microwave: A revised compilation. *J. Geophys. Res.* **2008**, *113*, D14220.

(7) Zasetsky, A. Y.; Khalizov, A. F.; Earle, M. E.; Sloan, J. J. Frequency Dependent Complex Refractive Indices of Supercooled Liquid Water and Ice Determined from Aerosol Extinction Spectra. *J. Phys. Chem. A* **2005**, *109*, 2760–2764.

(8) Malitson, I. H. Interspecimen Comparison of the Refractive Index of Fused Silica. *J. Opt. Soc. Am.* **1965**, *55*, 1205–1209.

(9) Zhuang, X.; Miranda, P. B.; Kim, D.; Shen, Y. R. Mapping molecular orientation and conformation at interfaces by surface nonlinear optics. *Phys. Rev. B* **1999**, *59*, 12632–12640.

(10) Bloembergen, N.; Pershan, P. S. Light Waves at the Boundary of Nonlinear Media. *Phys. Rev.* **1962**, *128*, 606–622.

(11) Sun, S.; Liang, R.; Xu, X.; Zhu, H.; Shen, Y. R.; Tian, C. Phase reference in phase-sensitive sum-frequency vibrational spectroscopy. *J. Chem. Phys.* **2016**, *144*, 244711.

(12) Wei, X.; Hong, S.-C.; Zhuang, X.; Goto, T.; Shen, Y. R. Nonlinear optical studies of liquid crystal alignment on a rubbed polyvinyl alcohol surface. *Phys. Rev. E* **2000**, *62*, 5160–5172.

(13) Hasegawa, T.; Tanimura, Y. A Polarizable Water Model for Intramolecular and Intermolecular Vibrational Spectroscopies. *J. Phys. Chem. B* **2011**, *115*, 5545–5553.

(14) Tuckerman, M.; Berne, B. J.; Martyna, G. J. Reversible multiple time scale molecular dynamics. *J. Chem. Phys.* **1992**, *97*, 1990–2001.

(15) Yoshida, H. Construction of higher order symplectic integrators. *Phys. Lett. A* **1990**, *150*, 262–268.

(16) Hoover, W. G. Canonical dynamics: Equilibrium phase-space distributions. *Phys. Rev. A* **1985**, *31*, 1695–1697.

(17) Nagata, Y.; Mukamel, S. Vibrational Sum-Frequency Generation Spectroscopy at the Water/Lipid Interface: Molecular Dynamics Simulation Study. *J. Am. Chem. Soc.* **2010**, *132*, 6434–6442.

(18) Nagata, Y.; Hsieh, C.-S.; Hasegawa, T.; Voll, J.; Backus, E. H. G.; Bonn, M. Water Bending Mode at the Water–Vapor Interface Probed by Sum-Frequency Generation Spectroscopy: A Combined Molecular Dynamics Simulation and Experimental Study. *J. Phys. Chem. Lett.* **2013**, *4*, 1872–1877.

(19) Berens, P. H.; Wilson, K. R. Molecular dynamics and spectra. I. Diatomic rotation and vibration. *J. Chem. Phys.* **1981**, *74*, 4872–4882.

(20) Medders, G. R.; Paesani, F. Dissecting the Molecular Structure of the Air/Water Interface from Quantum Simulations of the Sum-Frequency Generation Spectrum. *J. Am. Chem. Soc.* **2016**, *138*, 3912–3919.

(21) Nagata, Y.; Hasegawa, T.; Backus, E. H. G.; Usui, K.; Yoshimune, S.; Ohto, T.; Bonn, M. The surface roughness, but not the water molecular orientation varies with temperature at the water–air interface. *Phys. Chem. Chem. Phys.* **2015**, *17*, 23559–23564.

(22) Ohto, T.; Usui, K.; Hasegawa, T.; Bonn, M.; Nagata, Y. Toward ab initio molecular dynamics modeling for sum-frequency generation spectra; an efficient algorithm based on surface-specific velocity-velocity correlation function. *J. Chem. Phys.* **2015**, *143*, 124702.

(23) Schaefer, J.; Backus, E. H. G.; Nagata, Y.; Bonn, M. Both Inter- and Intramolecular Coupling of O–H Groups Determine the Vibrational Response of the Water/Air Interface. *J. Phys. Chem. Lett.* **2016**, *7*, 4591–4595.